Inorganic Chemistry

Article

pubs.acs.org/IC

Octadentate Zirconium(IV)-Loaded Macrocycles with Varied Stoichiometry Assembled From Hydroxamic Acid Monomers using Metal-Templated Synthesis

William Tieu,[†] Tulip Lifa,[†] Andrew Katsifis,[‡] and Rachel Codd*[,†]

[†]School of Medical Sciences (Pharmacology) and Bosch Institute, The University of Sydney, New South Wales 2006, Australia

[‡]Department of Molecular Imaging, Royal Prince Alfred Hospital, Camperdown, New South Wales 2050, Australia

Supporting Information

ABSTRACT: The reaction between Zr(IV) and the forward *endo*-hydroxamic acid monomer 4-[(5-aminopentyl)-(hydroxy)amino]-4-oxobutanoic acid (*for*-PBH) in a 1:4 stoichiometry in the presence of diphenylphosphoryl azide and triethylamine gave the octadentate Zr(IV)-loaded tetrameric hydroxamic acid macrocycle *for*-[Zr(DFOT$_1$)] ([M + H]$^+$ calc 887.3, obs 887.2). In this metal-templated synthesis (MTS) approach, the coordination preferences of Zr(IV) directed the preorganization of four oxygen-rich bidentate *for*-PBH ligands about the metal ion prior to ring closure under peptide coupling conditions. The replacement of *for*-PBH with 5-[(5-aminopentyl) (hydroxy)amino]-5-oxopentanoic acid (*for*-PPH), which contained an additional methylene group in the dicarboxylic acid region of the monomer, gave the analogous Zr(IV)-loaded macrocycle *for*-[Zr(PPDFOT$_1$)] ([M + H]$^+$ calc 943.4, obs 943.1). A second, well-resolved peak in the liquid chromatogram from the *for*-PPH MTS system also characterized as a species with [M + H]$^+$ 943.3, and was identified as the octadentate complex between Zr(IV) and two dimeric tetradentate hydroxamic acid macrocycles *for*-[Zr(PPDFOT$_{1D}$)$_2$]. Treatment of *for*-[Zr(PPDFOT$_1$)] or *for*-[Zr(PPDFOT$_{1D}$)$_2$] with EDTA at pH 4.0 gave the respective hydroxamic acid macrocycles as free ligands: octadentate PPDFOT$_1$ or two equivalents of tetradentate PPDFOT$_{1D}$ (homobisucaberin, HBC). At pH values closer to physiological, EDTA treatment of *for*-[Zr(DFOT$_1$)], *for*-[Zr(PPDFOT$_1$)], or Zr(IV) complexes with related linear tri- or tetrameric hydroxamic acid ligands showed the macrocycles were more resistant to the release of Zr(IV), which has implications for the design of ligands optimized for the use of Zr(IV)-89 in positron emission tomography (PET) imaging of cancer.

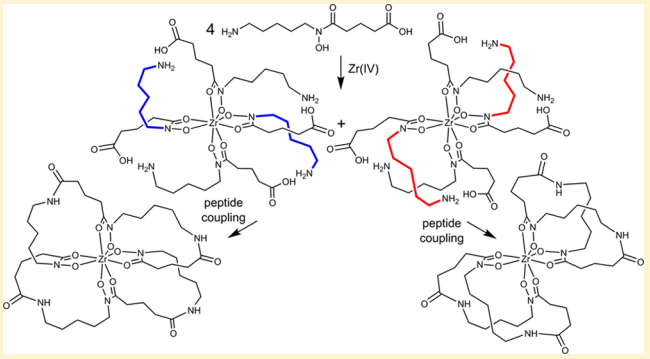

INTRODUCTION

Good clinical decision making in the diagnosis and management of patients with cancer is supported by access to high-definition images of the tumor with positron emission tomography (PET) imaging in wide use for this purpose.[1−4] Zirconium-89 has been under recent scrutiny as a radionuclide with properties that show promise for its use in antibody-coupled PET imaging.[5−9] The half-life of Zr-89 (3.27 d, β^+ = 22.7%, maximum β^+ energy = 0.897 MeV) is well-matched to the circulation half-life of antibodies, which makes Zr-89 attractive for immunological PET applications designed to concentrate the radionuclide at the site of the antigen-expressing tumor to improve the tumor-to-nontumor signal and the image resolution.[9−12] Progressing preclinical and clinical evaluation of Zr-89 as a PET radionuclide would benefit from a ligand suitably tailored to bind Zr(IV) with high affinity and selectivity. As a hard acid, Zr(IV) favors coordination with ligands rich in oxygen donor atoms,[13] which include hydroxamic acids.[14−16] The linear trimeric hydroxamic acid desferrioxamine B (Chart 1, **1**, DFOB), which is a metabolite of the siderophore class produced for Fe(III) acquisition by many *Streptomyces* species,[17−19] has been used to coordinate Zr-89 in a number of preclinical and clinical studies,[20−27] although as a hexadentate ligand, it is unable to saturate the preferred octadentate Zr(IV) coordination sphere.[28] The complex [Zr(DFOB)(OH$_2$)$_2$]$^+$ (Chart 1, **2**)[15,29] has only modest in vivo stability, which can result in the release and deposition of some of the radionuclide in nontargeted organs, and a reduction in the image quality.[29−31]

In recent work,[32,33] the DFOB scaffold was improved as a Zr(IV) ligand by undertaking a chain-extension reaction between DFOB and the *endo*-hydroxamic acid monomer 4-[(5-aminopentyl)(hydroxy)amino]-4-oxobutanoic acid (*for*-PBH), which is a biosynthetic fragment of desferrioxamine-type siderophores.[34−37] This produced a linear octadentate tetrameric hydroxamic acid ligand DFOB-*for*-PBH that formed [Zr(DFOB-*for*-PBH)] (Chart 1, **3**), which was more stable to

Received: February 9, 2017
Published: February 28, 2017

DOI: 10.1021/acs.inorgchem.7b00362
Inorg. Chem. 2017, 56, 3719−3728

Chart 1. Desferrioxamine B (DFOB) (1) and Its Complex with Zr(IV) (2)[a]

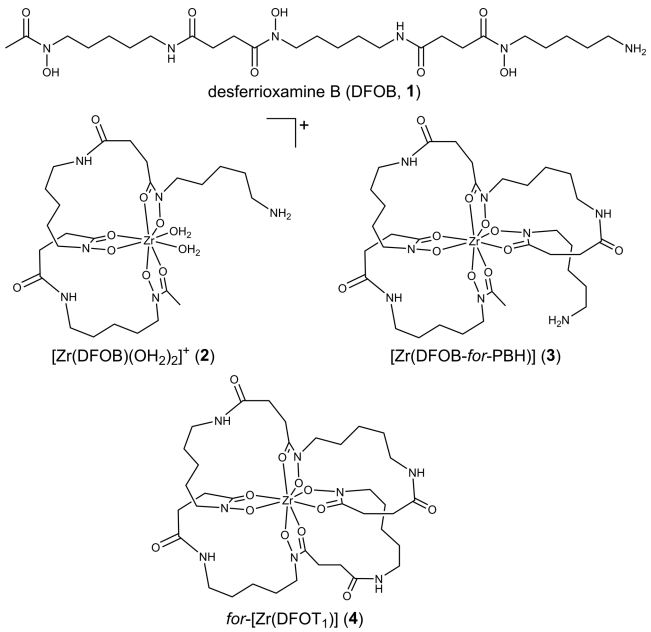

[a]Complexes between Zr(IV) and a linear (3) or macrocyclic (4) chain-extended variant of DFOB.

Zr(IV) release than $[Zr(DFOB)(OH_2)_2]^+$ (2). Complexes between Zr(IV) and other linear octadentate hydroxypyridinonate (HOPO)-type hydroxamic acid ligands[38−40] or a DFOB-squaramide ligand[41] have also been characterized. The current work considered that a further gain in the stability of the Zr(IV) complex could result if the octadentate DFOB-type tetrameric hydroxamic acid ligand was configured into a macrocycle (Chart 1, 4). This principle was supported by a study of macrocycles designed to coordinate Zr(IV) that were cyclized from hydrophobic abiological tetrameric linear constructs using ring-closing metathesis,[42] and from other studies focused upon developing macrocycles for Zr-89 PET imaging.[43]

The current work has used a metal-templated synthesis (MTS) approach to examine the ability of Zr(IV) to assemble its own best macrocycle from a selection of hydroxamic acid monomers reminiscent of the fragments used in siderophore biosynthesis. The stability of these macrocycles in retaining Zr(IV) could be reasonably compared to the linear tetrameric hydroxamic acid ligand DFOB-*for*-PBH, and trimeric DFOB. The use of a metal ion to template the assembly of its ideal coordination complex from a pool of fragment ligands that contain reactive termini is attractive in its simplicity, and offers the potential to deliver macrocycles with high affinity and selectivity.[44,45] Metal-templated synthesis (MTS) with Fe(III) or Ga(III) as the template has been used to assemble the trimeric hydroxamic acid macrocycle desferrioxamine E (DFOE) from *for*-PBH.[46] Other metal-loaded ring-expanded desferrioxamine-type macrocyclic siderophores have since been assembled using Fe(III) or Ga(III)-based MTS from a range of *endo*-hydroxamic acid monomers, including forward (*for*- = $H_2N-(CH_2)_x-N(OH)C(O)-(CH_2)_y-CO_2H$) and reverse (*ret*- = $H_2N-(CH_2)_x-C(O)N(OH)-(CH_2)_y-CO_2H$) ligands.[47]

In this work, the utility of MTS for assembling Zr(IV) macrocycles as constructs with potential relevance for Zr(IV)-89 PET imaging is reported. The importance of macrocycles in drug design,[48−51] warrants the development of new methods for the streamlined production of structurally diverse macrocycles.[52,53]

RESULTS AND DISCUSSION

Synthesis of *endo*-Hydroxamic Acid Ligands. A series of six *endo*-hydroxamic acid amino carboxylic acid monomers were prepared using reported methods: *for*-PBH, *for*-PPH, *for*-HBH, *ret*-PBH and *ret*-HBH.[47] The monomer 4-(6-amino-*N*-hydroxyhexanamido)butanoic acid (*ret*-PPH) was prepared in a fashion similar to *ret*-PBH, with the substitution of *tert*-butyl-3-[(benzyloxy)amino]propanoate with ethyl-4-[benzyloxy)-amino]butanoate (Scheme S1 and Figures S1−S6). The first letter in the nomenclature system for these ligands denotes the component derived from either pentane-1,5-diamine (P) or hexane-1,6-diamine (H), with the second letter referring to the component derived from butandioic acid (B) or pentandioic acid (P). The terminal 'H' is reference to the acidic proton of the hydroxamic acid. Native siderophores are assembled from forward (*for*-) *endo*-hydroxamic acids, which feature the internal −N(OH)C(O)− motif inserted in the direction as written, between the amine terminus and the carboxylic acid terminus. The reverse or *retro* (*ret*-) analogues feature the hydroxamic acid insert in the reverse orientation: −C(O)N-(OH)−. This work sought to determine whether Zr(IV) demonstrated a preference in the MTS-directed assembly of macrocycles from ligands that differed in length and thereby cavity size, as defined by the number of internal main-chain atoms (PBH, 10; PPH and HBH, 11); the position of the additional methylene group, as inserted in the diamine region (HBH) or the dicarboxylic acid region (PPH); and the orientation of the hydroxamic acid group (*for*-, *ret*-), which could affect the electronic structure and the physicochemical properties of the macrocycle (Scheme 1).

LC-MS Data From Zr(IV)-Based MTS Reaction Solutions. Standard MTS experiments involved the reaction between Zr(IV) and a given ligand (e.g., *for*-PBH) in a 1:4 ratio in a solution of 1:1 methanol:water to form the preassembled complex, with ring closure effected after a 5-d reaction time with diphenylphosphoryl azide (DPPA) and triethylamine. A series of three native tetrameric hydroxamic acid macrocycles has been characterized from cultures of *Erwinia amylovora*, with the macrocycle assembled from *for*-PBH named $DFOT_1$.[54] This naming system has been used here. The LC trace from the Zr(IV)-*for*-PBH MTS system showed a single peak (SIM 887) at t_R 29.7 min (Figure 1a), which in the MS gave an isotope pattern (Figure 2a) consistent with the calculated patterns (Figure 2d) of the $[M + 2H]^{2+}$, $[M + H]^+$, and $[M + Na]^+$ adducts of *for*-$[Zr(DFOT_1)]$ (4) (Scheme 1). The presence of Zr(IV) in the macrocycle was clear from the characteristic isotope pattern of natural Zr (^{90}Zr 51.45, ^{91}Zr 11.22, ^{92}Zr 17.15, ^{94}Zr 17.38, ^{96}Zr 2.80). Two other species were identified from the Zr(IV)-*for*-PBH MTS system, including the Zr(IV) complex formed with the linear tetrameric ligand ($[M + H]^+$ calc 905.4, obs 905.1), as the precursor of *for*-$[Zr(DFOT_1)]$ (4), and a trimeric Zr(IV)-loaded macrocycle ($[M]^+$ calc 687.2, obs 687.1). The latter species was confirmed as $[Zr(DFOE)]^+$ (with labile ancillary ligands (eg, H_2O) likely displaced during the MS procedure) from its coelution with an authentic sample of $[Zr(DFOE)]^+$ (Figure S7). No macrocycles were detected from a DPPA and triethylamine solution containing *for*-PBH in

DOI: 10.1021/acs.inorgchem.7b00362
Inorg. Chem. 2017, 56, 3719−3728

Scheme 1. Zr(IV)-Templated Synthesis of Tetrameric Macrocycles 4-9 from the Cognate Monomers *for*-PBH, *for*-PPH, *for*-HBH, *ret*-PBH, *ret*-PPH, or *ret*-HBH

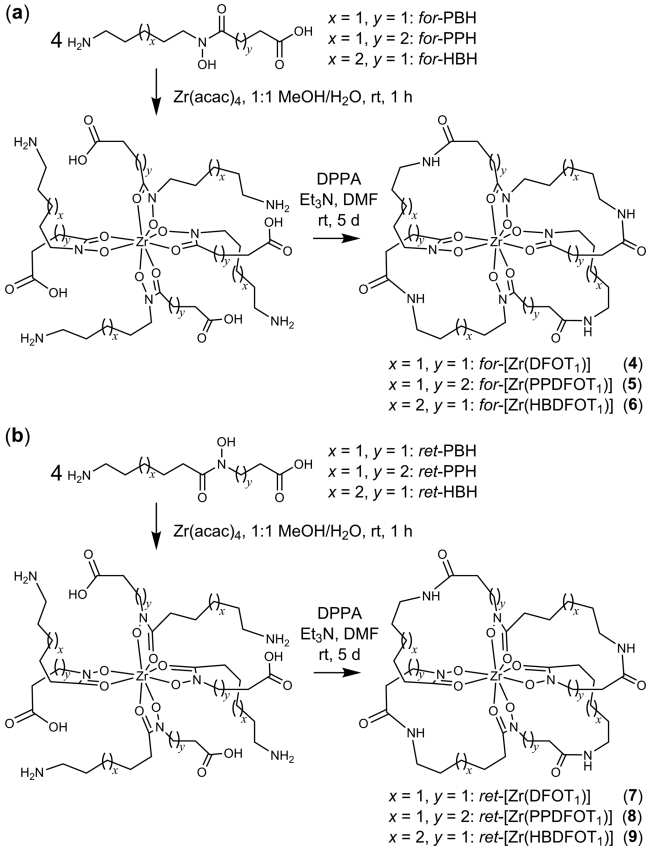

the absence of Zr(IV), which demonstrated the essential nature of the Zr(IV) ion template in the reaction.

In the Zr(IV)-*for*-PPH MTS system (SIM 943), two well-resolved peaks were present in the LC at t_R = 37.4 min and t_R = 42.7 min (Figure 1b). Each of these peaks gave experimental MS signals (t_R = 42.7 min, Figure 2b; t_R = 37.4 min, Figure 2c) that correlated with the presence of the $[M + 2H]^{2+}$, $[M + H]^+$, and $[M + Na]^+$ adducts of *for*-[Zr(PPDFOT$_1$)] (**5**) (calculated data Figure 2e–f). The presence of two peaks with identical MS characteristics was unexpected and was examined further in later experiments. The presence of four additional methylene groups in *for*-[Zr(PPDFOT$_1$)] (**5**) compared to *for*-[Zr(DFOT$_1$)] (**4**), was consistent with the increase of 56 m/z units in the $[M + H]^+$ adduct signal, with other adducts also showing consistent increases. Signals ascribable to the linear tetramer precursor of *for*-[Zr(PPDFOT$_1$)] (**5**) or the trimeric DFOE-type macrocyclic analogue were not detected in this system, or for any other monomer.

No LC peaks were discernible from the Zr(IV)-*for*-HBH (Figure 1c) or the Zr(IV)-*ret*-HBH (Figure 1f) MTS systems (SIM 943), which suggested that the formation of *for*-[Zr(HBDFOT$_1$)] (**6**) and *ret*-[Zr(HBDFOT$_1$)] (**9**) was unfavorable. The relative intensities of the LC peaks observed for the Zr(IV)-*ret*-PBH (Figure 1d) or the Zr(IV)-*ret*-PPH (Figure 1e) MTS systems to form macrocycles *ret*-[Zr(DFOT$_1$)] (**7**) or *ret*-[Zr(PPDFOT$_1$)] (**8**), respectively, was less than the corresponding *for*-PBH or *for*-PPH ligand systems, which indicated *for-endo*-hydroxamic acid monomers were favored above the *ret*-monomers in the Zr(IV)-macrocycle

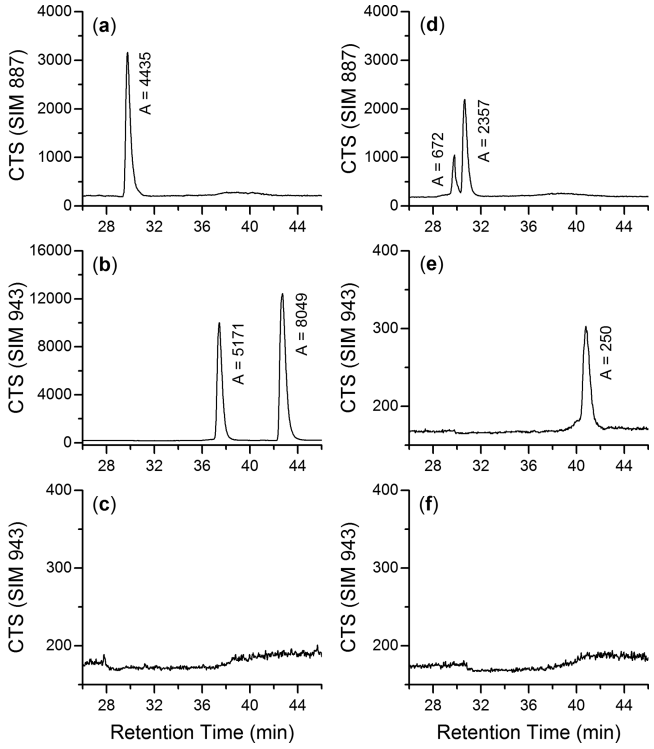

Figure 1. Liquid chromatograms from a solution of Zr(IV) and (a) *for*-PBH, (b) *for*-PPH, (c) *for*-HBH, (d) *ret*-PBH, (e) *ret*-PPH, or (f) *ret*-HBH, after reaction with peptide coupling reagents. Selected ion monitoring (SIM) was used as the detection mode, with values set to correspond with the $[M + H]^+$ adduct of the cognate macrocycle **4**–**9**.

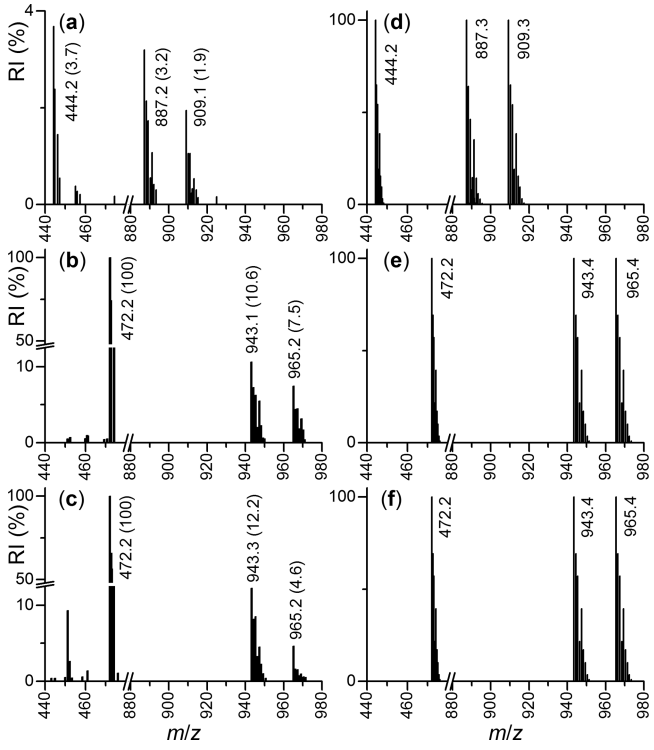

Figure 2. MS signals from the LC peaks detected using SIM values corresponding with (a) *for*-[Zr(DFOT$_1$)], and the two peaks consistent with *for*-[Zr(PPDFOT$_1$)] at (b) t_R = 42.7 min and (c) t_R = 37.4 min. The calculated isotope patterns for the corresponding species are aligned at right (d–f).

DOI: 10.1021/acs.inorgchem.7b00362
Inorg. Chem. 2017, 56, 3719–3728

formation. The LC trace from the Zr(IV)-*ret*-PBH MTS system was also resolved into two peaks, representing *ret*-[Zr(DFOT$_1$)] (**7**) and a second species of an uncertain nature. Peak integration gave a *for*-PBH/*ret*-PBH (sum of both peaks) ratio of 1.5, and a *for*-PPH/*ret*-PPH (sum of both peaks) ratio of 52.9.

Overall, the results demonstrated a degree of ligand selectivity was in operation in Zr(IV)-mediated macrocycle assembly. The use of MTS for the preparation of trimeric Fe(III)-loaded macrocycles,[47] showed a similar selectivity ratio with respect to the *for*-PBH/*ret*-PBH system. As distinct from the Zr(IV)-based MTS system, Fe(III)-loaded macrocycles were formed with *for*-HBH and *ret*-HBH, which demonstrated metal ion selectivity was in operation in the MTS systems.

Characterization of the Two Species in the Zr(IV)-*for*-PPH MTS System. The LC peaks for the higher-yielding Zr(IV)-MTS systems using *for*-PBH or *for*-PPH were collected for further characterization. The two peaks in the *for*-PPH system (Figure 1b) were collected separately and the integrity of the species confirmed by LC, with the species showing elution times of t_R = 35.5 min (Figure 3a) and 41.0 min (Figure 3g). The trace using TIC detection (black) was coincident with the trace (gray) using SIM values representative of *for*-[Zr(PPDFOT$_1$)] (**5**). The absolute retention times were different from the first acquired LC data, which was due to instrumental variation. To better understand the nature of the species, each fraction was incubated with EDTA at pH 4.0, with samples analyzed by LC-MS at 24 and 60 h. After 24 h, the earlier-eluting species gave a new signal using TIC detection at t_R = 28.1 min (Figure 3b), which gave an experimental MS isotope pattern (Figure 3e) consistent with the calculated pattern (Figure 3f) of $[M + 2H]^{2+}$, $[M + H]^+$ and $[M + Na]^+$ adducts of a Zr(IV)-free dimeric hydroxamic acid macrocycle assembled from two *for*-PPH units. After 60 h, the dimeric hydroxamic acid macrocycle remained present (Figure 3c, gray) with no remaining trace of the Zr(IV)-loaded parent species (Figure 3c, black). This supported that the earlier-eluting Zr(IV) species at t_R = 35.5 min was a complex of Zr(IV), in which the coordination sphere was saturated by two tetradentate dimeric macrocycles: *for*-[Zr(PPDFOT$_{1D}$)$_2$] (Scheme 2, **10**). The complex *for*-[Zr(PPDFOT$_{1D}$)$_2$] (**10**) was an isomer of *for*-[Zr(PPDFOT$_1$)] (**5**), in which the coordination sphere of the latter was saturated by one octadentate tetrameric macrocycle.

The dimeric macrocycle **11** released from EDTA-treated **10** is an analogue of the small family of dimeric hydroxamic acid macrocycles identified as natural bacterial siderophores, including alcaligin,[55] bisucaberin,[56] putrebactin,[57] and avaroferrin.[58−60] Since *for*-PPH contains one extra methylene group than *for*-PBH, which is the native monomer of the symmetric dimer bisucaberin, macrocycle **11** has been given the common name homobisucaberin (HBC).

After 24 h incubation with EDTA, the later-eluting Zr(IV) species gave a signal using TIC detection at t_R = 36.7 min (Figure 3h), with an experimental MS isotope pattern (Figure 3k) consistent with the calculated pattern of $[M + 2H]^{2+}$, $[M + H + Na]^{2+}$, $[M + H + K]^{2+}$, $[M + H]^+$, and $[M + Na]^+$ adducts (Figure 3l) of the apo-macrocycle PPDFOT$_1$ (**12**). There was a trace of *for*-[Zr(PPDFOT$_{1D}$)$_2$] (**10**) in this solution, which gave rise to a low intensity MS signal at *m*/*z* 451.2. After 60 h incubation, there remained traces of the parent *for*-[Zr(PPDFOT$_1$)] (**5**) (Figure 3i, black) in addition to the apo-macrocycle (gray). This demonstrated that the Zr(IV) ion was more readily removed from *for*-[Zr(PPDFOT$_{1D}$)$_2$] (**10**) than *for*-[Zr(PPDFOT$_1$)] (**5**). The extraction of Zr(IV) was pH dependent, with negligible Zr(IV) removed from *for*-[Zr(PPDFOT$_1$)] (**5**) at pH 7.0. An ^{1}H NMR spectrum of *for*-[Zr(PPDFOT$_1$)] (**5**) (Figure S8) showed signals that were clustered in regions similar to those observed for a Zr(IV)-DFOB complex,[39] although the signal complexity from conformational flux prevented the unambiguous assignment.

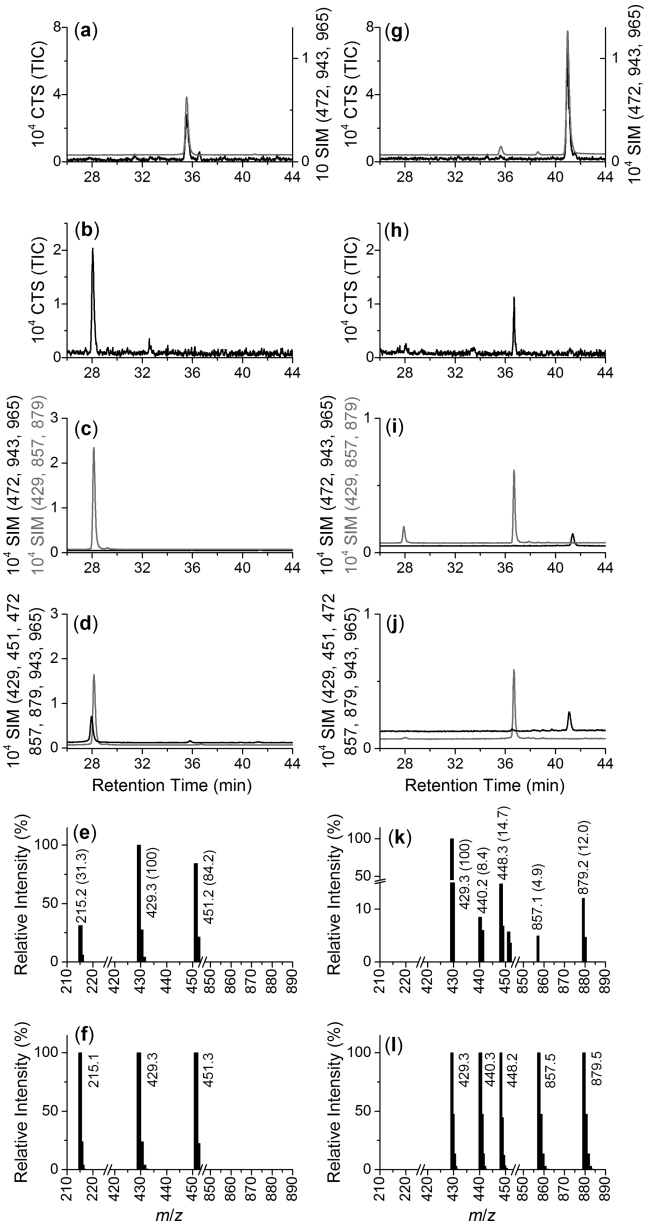

Figure 3. LC-MS data from a solution of **10** (column at left) or **5** (column at right), detected as (a, g) TIC (black) or at SIM values (gray) 472, 943, 965, corresponding to **5** and **10**, and following incubation with EDTA (pH 4), detected as (b, h) TIC, or (c, i) SIM values (black) 472, 943, 965, corresponding to **5** and **10**, or SIM values (gray) 429, 857, 879, corresponding to **11** and **12**, or after incubation of the peak at (d) 28.1 min (gray) or (j) 36.7 min (gray) with Zr(IV), detected as (d, j) SIM values (black) 429, 451, 472, 857, 879, 943, 965, corresponding with **5** and **10** and **11** and **12**. The MS signal from the peak at 28.1 min attributable to **11** is shown as experiment (e) or calculated (f); or at 36.7 min attributable to **12** as experiment (k) or calculated (l).

DOI: 10.1021/acs.inorgchem.7b00362
Inorg. Chem. 2017, 56, 3719−3728

Scheme 2. Zr(IV):*for*-PPH Complexes (1:4) Preorganized to Form *for*-[Zr(PPDFOT$_1$)] (5) or *for*-[Zr(PPDFOT$_{1D}$)$_2$] (10)[a]

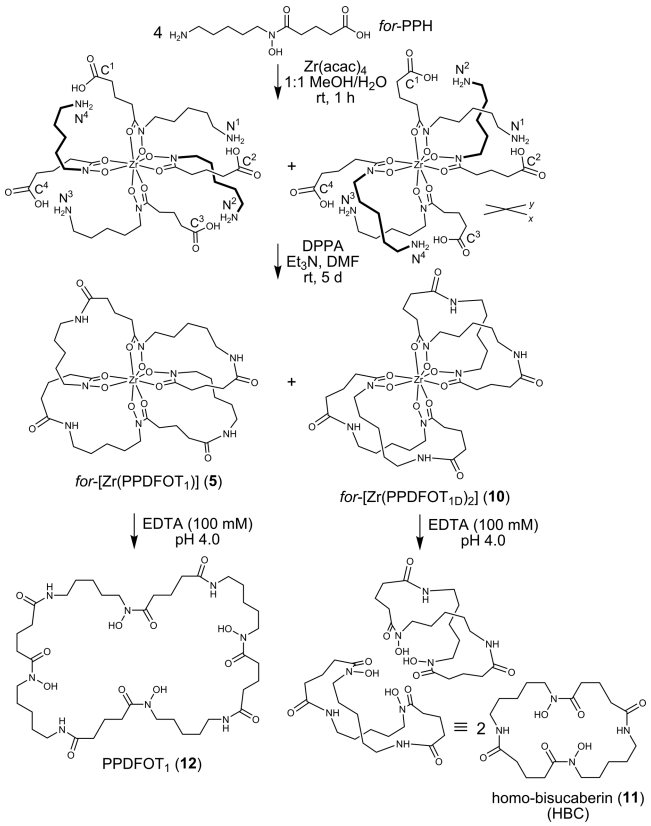

[a]Demetallation of 10 gave homo-bisucaberin **11**, and demetallation of 5 gave **12** in analytical yields.

The apo-macrocycles **11** and **12** were isolated and incubated with Zr(IV) to examine the reincorporation of Zr(IV), as a surrogate of the radiolabeling procedure. Incubation for 1 h of the dimeric hydroxamic acid macrocycle **11** with Zr(IV) did not reassemble *for*-[Zr(PPDFOT$_{1D}$)$_2$] (**10**), with the traces for the free ligand (Figure 3d, gray) and the solution following Zr(IV) incubation (Figure 3d, black) coincident. Incubation of the tetrameric hydroxamic apo-macrocycle PPDFOT$_1$ (**12**) (Figure 3j, gray) with Zr(IV) showed a signal (Figure 3j, black) that was coincident with *for*-[Zr(PPDFOT$_1$)] (**5**), which supported the viability of radiolabeling these types of macrocycles.

A repeat MTS reaction between Zr(IV) and *for*-PPH gave an LC trace with a similar distribution of [Zr(PPDFOT$_1$)] (**5**) and *for*-[Zr(PPDFOT$_{1D}$)$_2$] (**10**) (Figure S9) as first observed, supporting the reproducibility of the system. Each peak was isolated and a subsample subject to EDTA-based Zr(IV) removal (pH 4.0) and purification to give a sample set of the Zr(IV)-loaded macrocycles ([Zr(PPDFOT$_1$)] (**5**), *for*-[Zr(PPDFOT$_{1D}$)$_2$] (**10**)), and the corresponding apo-macrocycles (PPDFOT$_1$ (**12**), and HBC (**11**)) for analysis by high resolution MS. Each species analyzed in the HRMS as the [M + Na]$^+$ adduct, with HBC (**11**) showing an additional adduct [M]$^+$ attributable to a complex formed with adventitious Al^{3+} (Figure S10–S13).

The formation of *for*-[Zr(PPDFOT$_1$)] (**5**) would require coupling between the amine group of monomer 1 (N^1) and the DPPA-activated carboxylic acid group of monomer 2 (C^2); and contiguous coupling between N^2 and C^3, N^3 and C^4, and N^4 and C^1 (Scheme 2). As similar to *for*-[Zr(PPDFOT$_1$)] (**5**), the formation of *for*-[Zr(PPDFOT$_{1D}$)$_2$] (**10**) would require coupling between N^1 and C^2, but a second coupling between C^1 and N^2. The C^1–N^2 coupling would require the pendent amine group of monomer 2 to reorient from below the *x*-*y* plane to above the *x*-*y* plane. The other dimeric macrocycle comprising *for*-[Zr(PPDFOT$_{1D}$)$_2$] would be formed upon coupling between N^3 and C^4, as common to *for*-[Zr(PPDFOT$_1$)], and between C^3 and N^4, requiring the pendent amine group of monomer 4 move below the *x*-*y* plane (Scheme 2). In the case of the *for*-PPH MTS system, the distribution of both conformers as determined by probability, and the proximity of the relevant amine and activated carboxylic acid termini, were favorably poised to promote the formation of *for*-[Zr(PPDFOT$_1$)] (**5**) and *for*-[Zr(PPDFOT$_{1D}$)$_2$] (**10**). LC-MS analysis of the bulk solution from the *ret*-PBH MTS system following incubation with EDTA at pH 4.0 supported the presence of *ret*-[Zr(DFOT$_1$)] (**7**) and *ret*-[Zr(DFOT$_{1D}$)$_2$].

Molecular Mechanics Calculations. Structures of the Zr(IV) complexes with *for*-PBH, *for*-PPH or *for*-HBH to form a 1:1 Zr(IV):tetrameric macrocycle or a 1:2 Zr(IV):dimeric macrocycle were built using X-ray crystallographic data for [Zr(Me-AHA)$_4$] (Me-AHAH = *N*-methylacetohydroxamic acid)[15] as the core of the molecule, and fragments of *for*-PBH from the structure of [Fe(DFOB)] (Figure 4).[61] Molecular mechanics calculations showed that from the six complexes, *for*-[Zr(DFOT$_1$)] (**4**) gave the highest value for the minimum energy (Table 1), which was attributed to ring strain imposed by the suboptimal chain length of the *for*-PBH ligand. The average of the torsion angle of the four amide bonds was used as a surrogate measure of ring strain, with the value for *for*-[Zr(DFOT$_1$)] deviating the most from 180°. There was a significant decrease in the energy minimum for *for*-[Zr(DFOT$_{1D}$)$_2$], which was attributed to the reduction in the ring strain from *for*-[Zr(DFOT$_1$)] to the isomer *for*-[Zr(DFOT$_{1D}$)$_2$]. In each isomer pair of the 1:1 Zr(IV):tetrameric macrocycle and the 1:2 Zr(IV):dimeric macrocycle, the latter isomer gave a lower energy minimum, consistent with the notion that the organization of dimers reduced the ring strain in the octadentate complex. Molecular mechanics calculations using an alternative model of the Zr(IV) coordination sphere[42] gave high-energy structures of the dimer complexes, with one wing of the dimer partially inserted into the other, which supported the veracity of using the [Zr(Me-AHA)$_4$] core in the modeling.

As expected, the complexes modeled with *for*-PPH and *for*-HBH, that contained one additional methylene group than *for*-PBH, had greater volumes than *for*-[Zr(DFOT$_1$)] and *for*-[Zr(DFOT$_{1D}$)$_2$]. The energy minimum for *for*-[Zr(PPDFOT$_1$)] (**5**) was significantly less than *for*-[Zr(DFOT$_1$)] (**4**), which indicated that the additional methylene group in *for*-PPH was beneficial in the formation of a tetrameric macrocycle with a cavity size better optimized for the accommodation of the Zr(IV) ion. The reduced energy minimum for *for*-[Zr(PPDFOT$_1$)] (48 main-chain atoms) than *for*-[Zr(DFOT$_1$)] (44 main-chain atoms) could be considered more amplified than the absolute value, based on calibration to the number of main-chain atoms in the macrocycle, giving 11.6 or 14 kcal/mol per main-chain atom, respectively.

The structures of *for*-[Zr(PPDFOT$_1$)] and *for*-[Zr(PPDFOT$_{1D}$)$_2$] showed the amide oxygen atom was oriented away from the Zr(IV)-O_8 coordination sphere, with an average distance (as measured from each amide oxygen atom to the

DOI: 10.1021/acs.inorgchem.7b00362
Inorg. Chem. 2017, 56, 3719–3728

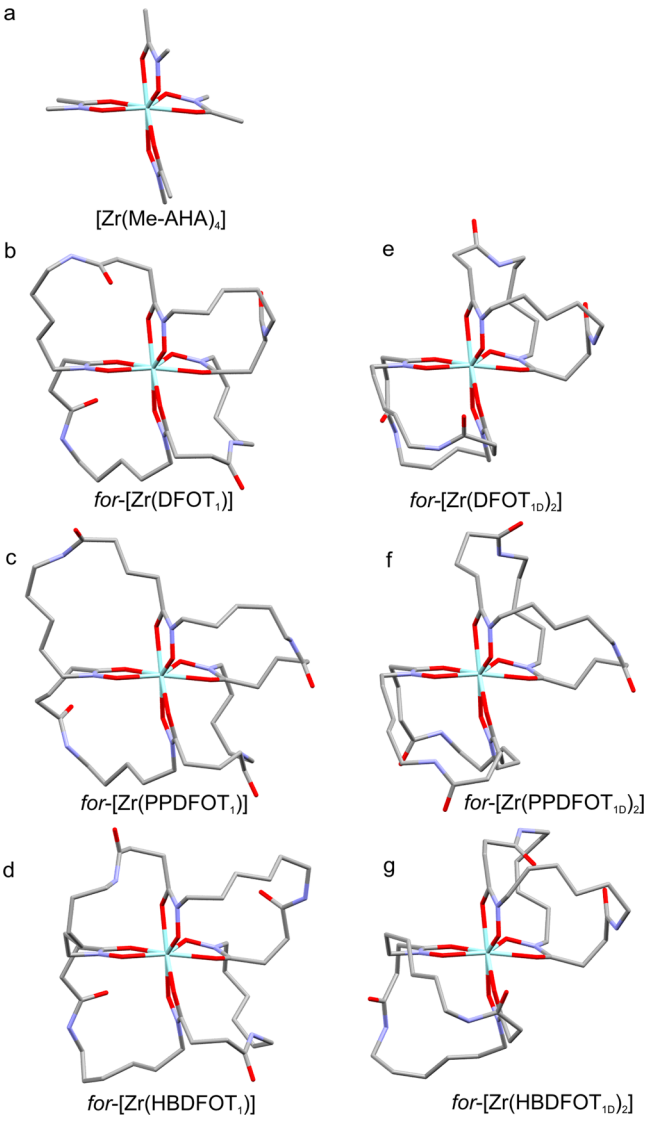

Figure 4. Structures of (a) Zr(IV)-$(Me\text{-}AHA)_4$ from X-ray crystallography[15] or from molecular mechanics calculations of the complex between Zr(IV) and a tetrameric macrocycle (Zr(IV):ligand 1:1) or the cognate dimeric macrocycle (Zr(IV):ligand 1:2) assembled from (b, e) *for*-PBH, (c, f) *for*-PPH, or (d, g) *for*-HBH.

Table 1. Data from Molecular Mechanics Calculations of the Zr(IV)-Loaded Macrocycles

complex	energy (kcal/mol)	vol. (Å^3)	θ_{amide} (deg)	distance CO_{amide}–CO/NO_{HX} (Å) av (n = 16)	distance CO_{amide}–CO/NO_{HX} (Å) min
for-[Zr(DFOT$_1$)]	563	1928	176.7	4.971	3.033
for-[Zr(DFOT$_{1D}$)$_2$]	544	1961	177.7	5.141	3.572
for-[Zr(PPDFOT$_1$)]	555	2113	178.2	6.478	4.756
for-[Zr(PPDFOT$_{1D}$)$_2$]	543	2173	178.2	6.346	4.859
for-[Zr(HBDFOT$_1$)]	552	2102	178.1	5.176	3.087
for-[Zr(HBDFOT$_{1D}$)$_2$]	551	2117	177.5	4.829	2.922

four oxygen donor atoms in the relevant quadrant) > 6.3 Å, with the minimum distance of about 4.7 Å. In the case of *for*-[Zr(DFOT$_1$)] and *for*-[Zr(DFOT$_{1D}$)$_2$] or *for*-[Zr(HBDFOT$_1$)] and *for*-[Zr(HBDFOT$_{1D}$)$_2$], there appeared to be a greater degree of steric and electronic repulsion resulting from the proximity of the amide oxygen atoms to the Zr(IV)-O_8 coordination sphere. These effects provide a possible rationale for the preference of the *for*-PPH ligand in the macrocycle assembly, and the lower concentration or no complex formation in the *for*-PBH and *for*-HBH ligand systems, respectively.

Release of Zr(IV) with EDTA Treatment. It was posited that in the presence of EDTA at physiological pH values, the Zr(IV) ion would be better retained by the Zr(IV)-loaded macrocycles, compared to related linear ligands. In the presence of a significant excess of EDTA, Zr(IV) was completely removed at pH 7.0 from $[Zr(DFOB)(OH_2)_2]^+$ (**2**) after 1 h incubation time (Figure 5). About 60% of Zr(IV) was retained

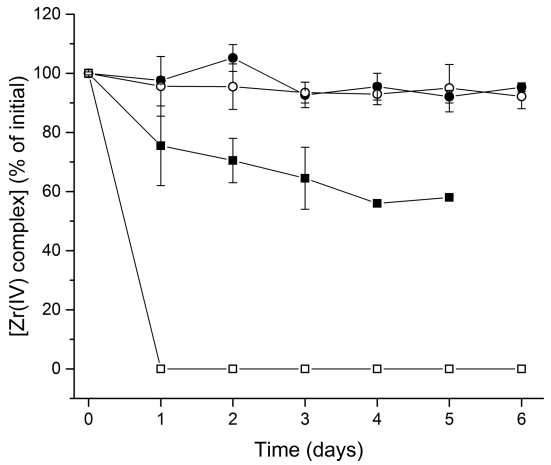

Figure 5. Percentage (n = 3) of initial concentration (LC-MS, SIM detection of the $[M]^+$ or $[M + H]^+$ adduct) of $[Zr(DFOB)]^+$ (open square), [Zr(DFOB-*for*-PBH)] (closed square; n = 1 for t = 4, 5 d), *for*-[Zr(DFOT$_1$)] (open circle) or *for*-[Zr(PPDFOT$_1$)] (closed circle) at t = 0, 1–6 days, in the presence of 1800 equiv of EDTA at pH 7.0.

in the linear, tetrameric chain-extended DFOB analogue [Zr(DFOB-*for*-PBH)] (**3**) after 72 h (refer to the ESI for the synthesis of DFOB-*for*-PBH, Figure S14). The trend in the increased stability of [Zr(DFOB-*for*-PBH)] (**3**) above $[Zr(DFOB)(OH_2)_2]^+$ (**2**) due to the increased ligand denticity was in agreement with previous work.[32] The current work showed a greater loss of Zr(IV) from [Zr(DFOB-*for*-PBH)] (**3**), which was ascribed to differences in reaction conditions and/or the use of a significant excess of EDTA, as was necessary for nonradioactive methods of detection. The loss of Zr(IV) from *for*-[Zr(DFOT$_1$)] (**4**) or *for*-[Zr(PPDFOT$_1$)] (**5**) was minimal under the same conditions, with 93% or 96% of the respective Zr(IV)-loaded macrocycles detected after 72 h. The minimal loss of Zr(IV) from *for*-[Zr(DFOT$_1$)] (**4**) and *for*-[Zr(PPDFOT$_1$)] (**5**) at pH 7.0 indicates the value that these types of macrocycles could have in Zr(IV)-89 PET imaging applications, to attenuate the loss of the Zr(IV)-89 radiolabel in vivo. The stability of the 44- or 48-membered macrocycles, *for*-[Zr(DFOT$_1$)] (**4**) or *for*-[Zr(PPDFOT$_1$)] (**5**), respectively, was in accord with previously reported Zr(IV) macrocycles.[42,43]

CONCLUSION

Reaction between Zr(IV) and a selection of *endo*-hydroxamic acid amino carboxylic acid ligands in a 1:4 stoichiometry in the presence of peptide coupling reagents was used to prepare Zr(IV)-loaded macrocycles. Of the six hydroxamic acid

DOI: 10.1021/acs.inorgchem.7b00362
Inorg. Chem. 2017, 56, 3719–3728

monomers examined using this MTS approach, *for*-PPH gave the highest concentration of Zr(IV)-loaded macrocycle, which was produced as an octadentate tetramer: *for*-[Zr(PPDFOT$_1$)] (**5**). An unexpected product was an octadentate Zr(IV)-loaded complex formed with two *for*-PPH derived dimeric macrocycles: *for*-[Zr(PPDFOT$_{1D}$)$_2$] (**10**). These two complexes are isomers. The MTS-based synthesis of *for*-[Zr(PPDFOT$_1$)] (**5**) was facile, albeit with the product formed in a modest yield (about 11%). MTS may have most value in identifying the ideal monomer required for the assembly of the optimal macrocycle, with more conventional synthetic methods,[62,63] including metal-ion-assisted ring closure,[64] required to obtain more material. MTS also has value in revealing new coordination chemistry for lesser known metal ions. The apo-macrocycles PPDFOT$_1$ (**12**) or homobisucaberin (HBC) (**11**) were obtained from the treatment of the respective compounds *for*-[Zr(PPDFOT$_1$)] (**5**) or *for*-[Zr(PPDFOT$_{1D}$)$_2$] (**10**) with EDTA at pH 4.0. Incubation of PPDFOT$_1$ with Zr(IV) for 1 h produced *for*-[Zr(PPDFOT$_1$)] (**5**). At pH values closer to physiological values, *for*-[Zr(DFOT$_1$)] (**4**) and *for*-[Zr-(PPDFOT$_1$)] (**5**) were stable toward the loss of Zr(IV), with the metal ion leached more readily from compounds containing linear hydroxamic acid–based ligands. The design of chelators that have high affinity and selectivity toward a given radionuclide is a field that is strongly coupled to the efficacy and clinical value of PET imaging.[1−4] The use of MTS to interrogate the coordination preferences of a given metal ion in the presence of a selection of fragment ligands, could have untapped potential in this regard. We are currently using MTS to inform optimal ligand design of a selection of frontier radionuclides, including Lu-177 and others.

EXPERIMENTAL SECTION

Reagents. The following chemicals were obtained from Sigma-Aldrich: ethyl 4-bromobutyrate (95%), *O*-benzylhydroxylamine hydrochloride (99%), Dowex 1 × 8 (Cl form), dimethyl sulfoxide (99.9%), diphenyl phosphoryl azide (97%), di-*tert*-butyl dicarbonate (Boc_2O; ≥98%), *tert*-butyl acrylate (98%), 1,5-dibromopentane (99%), potassium phthalimide (97%), triethylamine (TEA; 99%), *N*,*N*-dimethylformamide (DMF; 99.8%), 10% palladium on carbon, *N*,*N*-ethyldiisopropylamine (DIPEA; 99%), *tert*-butanol (≥99.0%), 1,4-dioxane (99.8%), tetrahydrofuran (THF; 99.8%), benzylchloroformate (95%), trifluoroacetic acid (TFA; ≥ 98%), sodium carbonate (99%), sodium hydride (60% suspension in oil), pyridine (99%), succinic anhydride (≥97%), glutaric anhydride (99%), 6-aminohexanoic acid (95%), 7-aminoheptanoic acid (98%), and magnesium sulfate ($MgSO_4$; 97%). Sodium sulfate ($NaSO_4$) and sodium bicarbonate (99.5%) were obtained from Chemsupply. Hydrazine hydrate ($N_2H_4\cdot H_2O$; 45−55%) was obtained from Ajax Chemicals. *N*-[3-(dimethylamino)propyl]-*N*′-ethylcarbodiimide hydrochloride (EDC·HCl; ≥ 98%), *N*-hydroxybenzotriazole (HOBt; ≥ 99%), and *N*-[(dimethylamino)-1*H*-1,2,3-triazolo-[4,5-*b*]pyridin-1-ylmethylene]-*N*-methylmethanaminium hexafluorophosphate *N*-oxide (HATU, 97%) were obtained from ChemImpex. Hydrogen (H_2) and nitrogen (N_2) gases were sourced from BOC. All chemicals were used as received. Milli-Q water was used for all experiments.

^{1}H NMR and ^{13}C NMR Spectroscopy. ^{1}H NMR and ^{13}C NMR spectroscopy was carried out using a Varian 400-MR NMR spectrometer (Lexington, MA) at a frequency of 399.73 MHz at 24 °C operated with VnmrJ 3.1 software (Agilent Technologies, Santa Clara, CA). The spectral data are reported in ppm (δ) relative to their residual solvent peaks for $CDCl_3$ (7.27 ppm (^{1}H), 77.23 ppm (^{13}C)) or CD_3OD (3.31 ppm, 4.87 ppm (^{1}H), 49.00 ppm (^{13}C)) or DMSO-d_6 (2.50 ppm (^{1}H), 39.52 ppm (^{13}C)). Coupling constants (J) are reported in Hz and splitting are reported as singlet (s), doublet (d), t (triplet), q (quartet), and qn (quintet).

Liquid Chromatography–Mass Spectrometry. Reverse-phase LC-MS was performed using an Agilent Technologies system (Santa Clara, CA), consisting of an injector (100 μL loop), Agilent 1260 Infinity degasser, a binary pump, a fraction collector, a diode array detector and an Agilent 6120 Series Quadrupole electrospray ionization (ESI)-mass spectrometer. An Agilent C18 column reverse-phased prepacked column (particle size: 5 μm; 4.6 × 150 mm internal diameter) was used at flow rate of 0.5 mL min^{-1}. Agilent OpenLAB Chromatography Data System (CDS) ChemStation Edition was used to process mass chromatograms in both the scan mode and the selected ion monitoring (SIM) mode. Two different gradients were used, as follows (A, H_2O/formic acid 99.9:0.1; B, ACN/formic acid 99.9:0.1). Method A: 0−42% B over 60 min (Figure 1, Figure 3, Figure S1). Method B: 0−15% B for 10 min, then 15−30% B over 35 min (semipreparative isolation of *for*-[Zr(PPDFOT$_1$)] and *for*-[Zr(PPDFOT$_{1D}$)]$_2$). MS isotope patterns were calculated using ChemCalc.[65]

Synthesis of Ligands. *for*-PBH, *for*-PPH, *for*-HBH, *ret*-PBH, and *ret*-HBH[34,47] or DFOB-*for*-PBH[32] were prepared as described previously. The ligand *ret*-PPH was prepared from precursors **P1**−**P4** (Scheme S1 and Figures S2−S5), with the final step undertaken from **P4** as follows.

4-(6-Amino-*N*-hydroxyhexanamido)butanoic acid (*ret*-PPH). A sample of **P4** (100 mg, 0.23 mmol) was dissolved in dichloromethane (4.5 mL) and trifluoroacetic acid (0.5 mL) was added. The reaction mixture was stirred for 3 h and concentrated *in vacuo* to give a yellow gum. The residue was dissolved in *tert*-butanol and ethyl acetate mixture (9:1, 5 mL) and 10% Pd/C was added under a nitrogen atmosphere. The mixture was purged with nitrogen, degassed, purged with hydrogen and then stirred under a hydrogen atmosphere for 8 h. The reaction mixture was quenched with water, filtered through cotton wool and concentrated in vacuo to give the title compound as a yellow gum. Yield: 86 mg, 93%. ^{1}H NMR (400 MHz, $CDCl_3$): δ 3.66 (t, J = 6.8 Hz, 2H), 2.93 (t, J = 7.6 Hz, 2H), 2.51 (t, J = 7.2 Hz, 2H), 2.32 (t, J = 7.2 Hz, 2H), 1.90 (apparent qn, J = 6.8 Hz, 2H), 1.62−1.69 (m, 4H), 1.39−1.47 (m, 2H) (Figure S6). ^{13}C NMR (101 MHz, $CDCl_3$): δ 176.9, 175.8, 49.9, 48.3, 40.5, 32.8, 32.0, 28.2, 27.0, 25.1, 23.1 (Figure S7).

Metal-Templated Synthesis. A 1:4 solution of Zr(IV) $(acac)_4$ and the *endo*-hydroxamic acid (2 mg/mL concentration with respect to the ligand) was prepared in 1:1 methanol/H_2O and the solution was stirred for 1 h. The mixture was concentrated to dryness in vacuo and was redissolved in DMF to a concentration of 1 mg/mL with respect to the ligand. Diphenylphosphoryl azide (6 equiv) and Et_3N (6 equiv) were added and the mixture was stirred at ambient temperature for 5 days. The reaction mixture was then quenched with cold H_2O (a volume equal to the volume of DMF). Aliquots (10 μL) were analyzed by LC-MS following HPLC method A. The mixture containing *for*-[Zr(DFOT$_1$)] or the mixture containing *for*-[Zr(PPDFOT$_1$)] and *for*-[Zr(PPDFOT$_{1D}$)$_2$] was further purified as follows. To the reaction mixture was added H_2O (10 mL per 1 mL reaction mixture) and Dowex 1 × 8 (0.1 g per 1 mL of reaction mixture) and was stirred for 24 h. The mixture was filtered and washed with 1:1 DMF/H_2O (2 × 50 mL), and the filtrate was concentrated in vacuo. The residue was redissolved in 1:1 DMSO/H_2O and purified by semipreparative HPLC following method C. Sufficient quantity of *for*-[Zr(PPDFOT$_1$)] was obtained for an ^{1}H NMR spectrum (400 MHz, $CDCl_3$): δ 8.39−8.46 (m, 2.3 H, exchange with solvent), 3.87−3.98 (m, 4H), 3.70−3.83 (m, 4H, 3.51−3.50 (m, 4H), 3.01−3.12 (m, 4H), 2.63−2.72 (m, 2H), 1.81−2.26 (m, 26H), 1.48−1.76 (m, 14H), 1.16−1.38 (m, 12H) (Figure S8).

Stability of Zr(IV) Complexes. Stock solutions (1 mg/mL) of *for*-[Zr(DFOT$_1$)] (**4**), *for*-[Zr(PPDFOT$_1$)] (**5**), *for*-[Zr(PPDFOT$_{1D}$)$_2$] (**10**), DFOB-*for*-PBH or DFOB were prepared in methanol. An aliquot (10 μL) of the stock solution of the relevant compound was added to an aliquot (190 μL) of EDTA (100 mM) at pH 4.0 (Figure 3) or pH 7.0 (Figure 5). Aliquots (10 μL) were removed at specified time points and the solutions were analyzed by LC-MS.

Reassembly of Zr(IV) Complexes. Solutions containing EDTA (171 μL, 100 mM) and *for*-[Zr(PPDFOT$_1$)] (**5**) (9 μL of 1 mg/mL)

DOI: 10.1021/acs.inorgchem.7b00362
Inorg. Chem. 2017, 56, 3719−3728

or *for*-[Zr(PPDFOT$_{1D}$)$_2$] (**10**) (9 μL of 1 mg/mL) were pH adjusted to 4.0 and after 60 h were purified by HPLC (Method A). PPDFOT$_1$ (**12**) was collected from 34.5−39.5 min and homobisucaberin (**11**) was collected from 26.5−29.5 min. The fractions were pooled, lyophilized and redissolved in Milli-Q water (200 μL). A sample of PPDFOT$_1$ (**12**) (10 μL) or homobisucaberin (**11**) was mixed with an aliquot (10 μL) of Zr(acac)$_4$ (0.25 mg/mL in 1:100 methanol:H$_2$O) and after incubation for 1 h was analyzed by LC-MS.

Molecular Mechanics Calculations. Structures of *for*-[Zr(DFOT$_1$)] and *for*-[Zr(DFOT$_{1D}$)$_2$] were built using HyperChem (version 7.5) from the X-ray coordinates of Zr(Me-AHA)$_4$[15] and fragments of *for*-PBH from Fe(III)-DFOB.[61] Additional methylene groups were inserted for *for*-[Zr(PPDFOT$_1$)], *for*-[Zr(PPDFOT$_{1D}$)$_2$], *for*-[Zr(HBDFOT$_1$)], and *for*-[Zr(HBDFOT$_{1D}$)$_2$]. Structures beyond atoms that included Zr(IV) and those in the first (O_8) and second (C_4N_4) coordination spheres were subject to energy minimization, using the AMBER2 force field. Further details and coordinates for all structures are provided (Table S1−S6).

■ ASSOCIATED CONTENT

Supporting Information

The Supporting Information is available free of charge on the ACS Publications website at DOI: 10.1021/acs.inorgchem.7b00362.

Data is provided for the synthesis of *ret*-PPH (Scheme 1, Figures S1−S6), the Zr(IV)-based *for*-PBH MTS system showing *for*-[Zr(DFOT$_1$)], the linear precursor of *for*-[Zr(DFOT$_1$)] and [Zr(DFOE)]$^+$ (Figure S7), the ^{1}H NMR spectrum of *for*-[Zr(PPDFOT$_1$)] (Figure S8); the repeat MTS-based synthesis with *for*-PPH (Figure S9); HRMS data for *for*-[Zr(PPDFOT$_1$)], *for*-[Zr(PPDFOT$_{1D}$)$_2$], PPDFOT$_1$ or PPDFOT$_{1D}$ (HBC) (Figures S10−13, respectively); the ^{1}H NMR spectrum of DFOB-*for*-PBH (Figure S14); and the coordinates of the structures of *for*-[Zr(DFOT$_1$)], *for*-[Zr(DFOT$_{1D}$)$_2$], *for*-[Zr(PPDFOT$_1$)], *for*-[Zr(PPDFOT$_{1D}$)$_2$], *for*-[Zr(HBDFOT$_1$)], and *for*-[Zr(HBDFOT$_{1D}$)$_2$] (Tables S1−S6) (PDF)

■ AUTHOR INFORMATION

Corresponding Author

*E-mail: rachel.codd@sydney.edu.au.

ORCID

Rachel Codd: 0000-0002-2703-883X

Notes

The authors declare no competing financial interest.

■ ACKNOWLEDGMENTS

The Australian Research Council (DP140100092) is acknowledged for research support to R.C. and A.K. and for salary support to W.T. The University of Sydney is acknowledged for the provision of a postgraduate research award (cofunded) to T.L.

■ REFERENCES

(1) Price, E. W.; Orvig, C. Matching chelators to radiometals for radiopharmaceuticals. *Chem. Soc. Rev.* **2014**, *43*, 260−290.

(2) Zeglis, B. M.; Houghton, J. L.; Evans, M. J.; Viola-Villegas, N.; Lewis, J. S. Underscoring the influence of inorganic chemistry on nuclear imaging with radiometals. *Inorg. Chem.* **2014**, *53*, 1880−1899.

(3) Price, T. W.; Greenman, J.; Stasiuk, G. J. Current advances in ligand design for inorganic positron emission tomography tracers 68Ga, 64Cu, 89Zr and 44Sc. *Dalton Trans.* **2016**, *45*, 15702−15724.

(4) Boros, E.; Marquez, B. V.; Ikotun, O. F.; Lapi, S. E.; Ferreira, C. L. In *Ligand Design in Medicinal Inorganic Chemistry*; Storr, T., Ed.; John Wiley & Sons, Ltd: Chichester, UK, 2014.

(5) Fischer, G.; Seibold, U.; Schirrmacher, R.; Wängler, B.; Wängler, C. ^{89}Zr, a radiometal nuclide with high potential for molecular imaging with PET: chemistry, applications and remaining challenges. *Molecules* **2013**, *18*, 6469−6490.

(6) Blower, P. J. A nuclear chocolate box: the periodic table of nuclear medicine. *Dalton Trans.* **2015**, *44*, 4819−4844.

(7) Brasse, D.; Nonat, A. Radiometals: towards a new success story in nuclear imaging. *Dalton Trans.* **2015**, *44*, 4845−4858.

(8) van Dongen, G. A. M. S.; Huisman, M. C.; Boellaard, R.; Hendrikse, N. H.; Windhorst, A. D.; Visser, G. W. M.; Molthoff, C. F. M.; Vugts, D. J. 89Zr-immuno-PET for imaging of long circulating drugs and disease targets: why, how and when to be applied? *Q. J. Nucl. Med. Mol. Imaging* **2015**, *59*, 18−38.

(9) Scharli, R. K.; Price, R. I.; Chan, S.; Cryer, D.; Jeffery, C. M.; Asad, A. H.; Morandeau, L.; Eu, P.; Cullinane, C.; Kasbollah, A.; Katsifis, A. Establishing reliable production of the PET isotope 89Zr for research use: From target fabrication to preclinical imaging. *AIP Conf. Proc.* **2012**, *1509*, 101−107.

(10) Verel, I.; Visser, G. W. M.; Boellaard, R.; Stiger-van Walsum, M.; Snow, G. B.; van Dongen, G. A. M. S. ^{89}Zr immuno-PET: Comprehensive procedures for the production of ^{89}Zr-labeled monoclonal antibodies. *J. Nucl. Med.* **2003**, *44*, 1271−1281.

(11) Rice, S. L.; Roney, C. A.; Daumar, P.; Lewis, J. A. The next generation of positron emission tomography radiopharmaceuticals in oncology. *Semin. Nucl. Med.* **2011**, *41*, 265−282.

(12) Deri, M. A.; Zeglis, B. M.; Francesconi, L. C.; Lewis, J. S. PET imaging with 89Zr: From radiochemistry to the clinic. *Nucl. Med. Biol.* **2013**, *40*, 3−14.

(13) Baggio, R.; Garland, M. T.; Perec, M. Preparation and X-ray crystal structure of the polymeric zirconium(IV) oxalate complex $[K_2\{Zr(C_2O_4)_3\}\cdot H_2C_2O_4\cdot H_2O]_n$. *Inorg. Chem.* **1997**, *36*, 737−739.

(14) Baroncelli, F.; Grossi, G. The complexing power of hydroxamic acids and its effect on the behaviour of organic extractants in the reprocessing of irradiated fuels. I. The complexes between benzohydroxamic acid and zirconium, iron(III) and uranium(IV). *J. Inorg. Nucl. Chem.* **1965**, *27*, 1085−1092.

(15) Guérard, F.; Lee, Y.-S.; Tripier, R.; Szajek, L. P.; Deschamps, J. R.; Brechbiel, M. W. Investigation of Zr(IV) and ^{89}Zr(IV) complexation with hydroxamates: progress towards designing a better chelator than desferrioxamine B for immuno-PET imaging. *Chem. Commun.* **2013**, *49*, 1002−1004.

(16) Codd, R. Traversing the coordination chemistry and chemical biology of hydroxamic acids. *Coord. Chem. Rev.* **2008**, *252*, 1387−1408.

(17) Hider, R. C.; Kong, X. Chemistry and biology of siderophores. *Nat. Prod. Rep.* **2010**, *27*, 637−657.

(18) Braich, N.; Codd, R. Immobilized metal affinity chromatography for the capture of hydroxamate-containing siderophores and other Fe(III)-binding metabolites from bacterial culture supernatants. *Analyst* **2008**, *133*, 877−880.

(19) Ejje, N.; Soe, C. Z.; Gu, J.; Codd, R. The variable hydroxamic acid siderophore metabolome of the marine actinomycete *Salinispora tropica* CNB-440. *Metallomics* **2013**, *5*, 1519−1528.

(20) Meijs, W. E.; Herscheid, J. D. M.; Haisma, H. J.; Pinedo, H. M. Evaluation of desferal as a bifunctional chelating agent for labeling antibodies with Zr-89. *Appl. Radiat. Isot.* **1992**, *43*, 1443−1447.

(21) Meijs, W. E.; Haisma, H. J.; Klok, R. P.; van Gog, F. B.; Kievit, E.; Pinedo, H. M.; Herscheid, J. D. Zirconium-labeled monocloncal antibodies and their distribution in tumor-bearing nude mice. *J. Nucl. Med.* **1997**, *38*, 112−118.

(22) Börjesson, P. K. E.; Jauw, Y. W. S.; Boellaard, R.; de Bree, R.; Comans, E. F. I.; Roos, J. C.; Castelijns, J. A.; Vosjan, M. J. W. D.; Kummer, J. A.; Leemans, C. R.; Lammertsma, A. A.; van Dongen, G. A. M. S. Performance of immuno-positron emission tomography with zirconium-89-labeled chimeric monoclonal antibody U36 in the detection of lymph node metastases in head and neck cancer patients. *Clin. Cancer Res.* **2006**, *12*, 2133−2140.

DOI: 10.1021/acs.inorgchem.7b00362
Inorg. Chem. 2017, 56, 3719−3728

(23) van Rij, C. M.; Sharkey, R. M.; Goldenberg, D. M.; Frielink, C.; Molkenboer, J. D.; Franssen, G. M.; van Weerden, W. M.; Oyen, W. J.; Boerman, O. C. Imaging of prostate cancer with immuno-PET and immuno-SPECT using a radiolabeled anti-EPG-1 monoclonal antibody. *J. Nucl. Med.* **2011**, *52*, 1601−1607.
(24) Dijkers, E. C. F.; Kosterink, J. G. W.; Rademaker, A. P.; Perk, L. R.; van Dongen, G. A. M. S.; Bart, J.; de Jong, J. R.; de Vries, E. G. E.; Lub-de Hooge, M. N. Development and characterisation of clinical-grade ^{89}Zr-trastuzumab for HER2/*neu* imminoPET imaging. *J. Nucl. Med.* **2009**, *50*, 974−981.
(25) Holland, J. P.; Caldas-Lopes, E.; Divilov, V.; Longo, V. A.; Taldone, T.; Zatorska, D.; Chiosis, G.; Lewis, J. S. Measuring the pharmacodynamic effects of a novel Hsp90 inhibitor on HER2/*neu* expression in mice using ^{89}Zr-DFO-trastuzumab. *PLoS One* **2010**, *5*, e8859.
(26) Petrik, M.; Zhai, C.; Novy, Z.; Urbanek, L.; Haas, H.; Decristoforo, C. *In vitro* and *in vivo* comparison of selected Ga-68 adn Zr-89 labelled siderophores. *Mol. Imaging Biol.* **2016**, *18*, 344−352.
(27) Jauw, Y. W. S.; Menke-van der Houven van Oordt, C. W.; Hoekstra, O. S.; Hendrikse, N. H.; Vugts, D. J.; Zijlstra, J. M.; Huisman, M. C.; van Dongen, G. A. M. S. Immuno-positron emission tomography with zirconium-89-labeled monoclonal antibodies in oncology: waht can we learn from initial clinical trials? *Front. Pharmacol.* **2016**, *7* (131), 15.
(28) Holland, J. P.; Vasdev, N. Charting the mechanism and reactivity of zirconium oxalate with hydroxamate ligands using density functional theory: Implications in new chelate design. *Dalton Trans.* **2014**, *43*, 9872−9884.
(29) Holland, J. P.; Divilov, V.; Bander, N. H.; Smith-Jones, P. M.; Larson, S. M.; Lewis, J. S. ^{89}Zr-DFO-J591 for immunoPET of prostate-specific membrane antigen expression *in vivo*. *J. Nucl. Med.* **2010**, *51*, 1293−1300.
(30) Abou, D. S.; Ku, T.; Smith-Jones, P. M. *In vivo* biodistribution and accumulation of ^{89}Zr in mice. *Nucl. Med. Biol.* **2011**, *38*, 675−681.
(31) Nayak, T. K.; Garmestani, K.; Milenic, D. E.; Brechbiel, M. W. PET and MRI of metastatic peritoneal and pulmonary colorectal cancer in mice with human epidermal growth factor receptor 1-targeted 89Zr-labeled panitumumab. *J. Nucl. Med.* **2012**, *53*, 113−120.
(32) Patra, M.; Bauman, A.; Mari, C.; Fischer, C. A.; Blacque, O.; Haussinger, D.; Gasser, G.; Mindt, T. L. An octadentate bifunctional chelating agent for the development of stable zirconium-89 based molecular imaging probes. *Chem. Commun.* **2014**, *50*, 11523−11525.
(33) Vugts, D. J.; Klaver, C.; Sewing, C.; Poot, A. J.; Adamzek, K.; Huegli, S.; Mari, C.; Visser, G. W. M.; Valverde, I. E.; Gasser, G.; Mindt, T. L.; van Dongen, G. A. M. S. Comparison of the octadentate bifunctional chelator DFO*-*p*Phe-NCS and the clinically used hexadentate bifunctional chelator DFO-*p*Phe-NCS for 89-Zr-immuno-PET. *Eur. J. Nucl. Med. Mol. Imaging* **2017**, *44*, 286−295.
(34) Kadi, N.; Oves-Costales, D.; Barona-Gomez, F.; Challis, G. L. A new family of ATP-dependent oligomerization-macrocyclization biocatalysts. *Nat. Chem. Biol.* **2007**, *3*, 652−656.
(35) Soe, C. Z.; Codd, R. Unsaturated macrocyclic dihydroxamic acid siderophores produced by *Shewanella putrefaciens* using precursor-directed biosynthesis. *ACS Chem. Biol.* **2014**, *9*, 945−956.
(36) Telfer, T. J.; Gotsbacher, M. P.; Soe, C. Z.; Codd, R. Mixing up the pieces of the desferrioxamine B jigsaw defines the biosynthetic sequence catalyzed by DesD. *ACS Chem. Biol.* **2016**, *11*, 1452−1462.
(37) Richardson-Sanchez, T.; Tieu, W.; Codd, R. Reverse biosynthesis: Generating combinatorial pools of drug leads from enzyme-mediated fragmentation of natural products. *ChemBioChem* **2017**, *18*, 368−373.
(38) Deri, M. A.; Ponnala, S.; Zeglis, B. M.; Pohl, G.; Dannenberg, J. J.; Lewis, J. S.; Francesconi, L. C. Alternative chelator for ^{89}Zr radiopharmaceuticals: radiolabeling and evaluation of 3,4,3,-(LI-1,2-HOPO). *J. Med. Chem.* **2014**, *57*, 4849−4860.
(39) Ma, M. T.; Meszaros, L. K.; Paterson, B. M.; Berry, D. J.; Cooper, M. S.; Ma, Y. M.; Hider, R. C.; Blower, P. J. Tripodal tris(hydroxypyridinone) ligands for immunoconjugate PET imaging with ^{89}Zr^{4+}: Comparison with desferrioxamine B. *Dalton Trans.* **2015**, *44*, 4884−4900.
(40) Deri, M. A.; Ponnala, S.; Kozlowski, P.; Burton-Pye, B. P.; Cicek, H. T.; Hu, C.; Lewis, J. S.; Francesconi, L. C. p-SCN-Bn-HOPO: a superior bifunctional chelator for 89Zr immunoPET. *Bioconjugate Chem.* **2015**, *26*, 2579−2591.
(41) Rudd, S. E.; Roselt, P.; Cullinane, C.; Hicks, R. J.; Donnelly, P. S. A desferrioxmaine B squaramide ester for the incorporation of zirconium-89 into antibodies. *Chem. Commun.* **2016**, *52*, 11889−11892.
(42) Guérard, F.; Lee, Y.-S.; Brechbiel, M. W. Rational design, synthesis, and evaluation of tetrahydroxamic acid chelators for stable complexation of zirconium(IV). *Chem. - Eur. J.* **2014**, *20*, 5584−5591.
(43) Boros, E.; Holland, J. P.; Kenton, N.; Rotile, N. J.; Caravan, P. Macrocycle-based hydroxamate ligands for complexation and immunoconjugation of 89zirconium for positron emission tomography (PET) imaging. *ChemPlusChem* **2016**, *81*, 274−281.
(44) McMurry, T. J.; Raymond, K. N.; Smith, P. H. Molecular recognition and metal ion template synthesis. *Science* **1989**, *244*, 938−943.
(45) McMurry, T. J.; Rodgers, S. J.; Raymond, K. N. Template and stepwise synthesis of a macrobicyclic catechoylamide ferric ion sequestering agent. *J. Am. Chem. Soc.* **1987**, *109*, 3451−3453.
(46) Kachadourian, R.; Chuilon, S.; Mérienne, C.; Kunesch, G.; Deroussent, A. A New Total Synthesis of Ferrioxamine E through Metal-templated Cyclic Trimerization. *Supramol. Chem.* **1997**, *8*, 301−308.
(47) Lifa, T.; Tieu, W.; Hocking, R. K.; Codd, R. Forward and reverse (*retro*) iron(III)- or gallium(III)-desferrioxamine E and ring-expanded analogs prepared using metal-templated synthesis from *endo*-hydroxamic acid monomers. *Inorg. Chem.* **2015**, *54*, 3573−3583.
(48) Giordanetto, F.; Kihlberg, J. Macrocyclic drugs and clinical candidates: What can medicinal chemists learn from their properties? *J. Med. Chem.* **2014**, *57*, 278−294.
(49) Driggers, E. M.; Hale, S. P.; Lee, J.; Terrett, N. K. The exploration of macrocycles for drug discovery - an underexploited structural class. *Nat. Rev. Drug Discovery* **2008**, *7*, 608−624.
(50) Marsault, E.; Peterson, M. L. Macrocycles are great cycles: Applications, opportunities, and challenges of synthethic macrocycles in drug discovery. *J. Med. Chem.* **2011**, *54*, 1961−2004.
(51) Heinis, C. Drug discovery. Tools and rules for macrocycles. *Nat. Chem. Biol.* **2014**, *10*, 696−698.
(52) Marti-Centelles, V.; Pandey, M. D.; Burguete, M. I.; Luis, S. V. Macrocyclization reactions: the importance of conformational, configurational, and template-induced preorganisation. *Chem. Rev.* **2015**, *115*, 8736−8834.
(53) Marti-Centelles, V.; Burguete, M. I.; Luis, S. V. Macrocycle synthesis by chloride-templated amide bond formation. *J. Org. Chem.* **2016**, *81*, 2143−2147.
(54) Feistner, G. J.; Stahl, D. C.; Gabrik, A. H. Proferrioxamine siderophores of *Erwinia amylovora*. A capillary liquid chromatographic/electrospray tandem mass spectrometric study. *Org. Mass Spectrom.* **1993**, *28*, 163−175.
(55) Nishio, T.; Tanaka, N.; Hiratake, J.; Katsube, Y.; Ishida, Y.; Oda, J. Isolation and structure of the novel dihydroxamate siderophore alcaligin. *J. Am. Chem. Soc.* **1988**, *110*, 8733−8734.
(56) Takahashi, A.; Nakamura, H.; Kameyama, T.; Kurasawa, S.; Naganawa, H.; Okami, Y.; Takeuchi, T.; Umezawa, H.; Iitaka, Y. Bisucaberin, a new siderophore, sensitizing tumor cells to macrophage-mediated cytolysis. II. Physico-chemical properties and structure determination. *J. Antibiot.* **1987**, *40*, 1671−1676.
(57) Ledyard, K. M.; Butler, A. Structure of putrebactin, a new dihydroxamate siderophore produced by *Shewanella putrefaciens*. *JBIC, J. Biol. Inorg. Chem.* **1997**, *2*, 93−97.
(58) Soe, C. Z.; Pakchung, A. A. H.; Codd, R. Directing the biosynthesis of putrebactin or desferrioxamine B in *Shewanella putrefaciens* through the upstream inhibition of ornithine decarboxylase. *Chem. Biodiversity* **2012**, *9*, 1880−1890.

DOI: 10.1021/acs.inorgchem.7b00362
Inorg. Chem. 2017, 56, 3719−3728

(59) Boettcher, T.; Clardy, J. A chimeric siderophore halts swarming *Vibrio*. *Angew. Chem., Int. Ed.* **2014**, *53*, 3510−3513.
(60) Soe, C. Z.; Telfer, T. J.; Levina, A.; Lay, P. A.; Codd, R. Simultaneous biosynthesis of putrebactin, avaroferrin and bisucaberin by *Shewanella putrefaciens* and characterisation of complexes with iron(III), molybdenum(VI) or chromium(V). *J. Inorg. Biochem.* **2016**, *162*, 207−215.
(61) Dhungana, S.; White, P. S.; Crumbliss, A. L. Crystal structure of ferrioxamine B: A comparative analysis and implications for molecular recognition. *JBIC, J. Biol. Inorg. Chem.* **2001**, *6*, 810−818.
(62) Bergeron, R. J.; McManis, J. S. The total synthesis of desferrioxamines E and G. *Tetrahedron* **1990**, *46*, 5881−5888.
(63) Bergeron, R. J.; McManis, J. S.; Phanstiel, O. I.; Vinson, J. R. T. A versatile synthesis of deferrioxamine B. *J. Org. Chem.* **1995**, *60*, 109−114.
(64) Wencewicz, T. A.; Oliver, A. G.; Miller, M. J. Iron(III)-templated macrolactonization of trihydroxamate siderophores. *Org. Lett.* **2012**, *14*, 4390−4393.
(65) Patiny, L.; Borel, A. ChemCalc: a building block for tomorrow's chemical infrastructure. *J. Chem. Inf. Model.* **2013**, *53*, 1223−1228.

DOI: 10.1021/acs.inorgchem.7b00362
Inorg. Chem. 2017, 56, 3719−3728